Article

Development and Validation of a CFD Combustion Model for Natural Gas Engines Operating with Different Piston Bowls

Giovanni Gaetano Gianetti [1], **Tommaso Lucchini** [1], **Gianluca D'Errico** [1], **Angelo Onorati** [1,*] and **Patrik Soltic** [2]

1   ICE Group—Politecnico di Milano, 20156 Milan, Italy
2   Empa Automotive Powertrain Technologies, 8600 Dübendorf, Switzerland
*   Correspondence: angelo.onorati@polimi.it

Abstract: Nowadays, an accurate and precise description of the combustion phase is essential in spark-ignition (SI) engines to drastically reduce pollutant and greenhouse gas (GHG) emissions and increase thermal efficiency. To this end, computational fluid dynamics (CFD) can be used to study the different phenomena involved, such as the ignition of the charge, combustion development, and pollutant formation. In this work, a validation of a CFD methodology based on the flame area model (FAM) was carried out to model the combustion process in light-duty SI engines fueled with natural gas. A simplified spherical kernel approach was used to model the ignition phase, whereas turbulent flame propagation was described through two variables. A zero-dimensional evolution of the flame kernel radius was used in combination with the Herweg and Maly formulation to take the laminar-to-turbulent flame transition into account. To estimate the chemical composition of burnt gas, two different approaches were considered—one was based on tabulated kinetics, and the other was based on chemical equilibrium. Assessment of the combustion model was first performed by using different operating points of a light-duty SI engine fueled with natural gas and by using the original piston. The results were validated by using experimental data on the in-cylinder pressure, apparent heat release rate, and pollutant emissions. Afterward, two other different piston bowl geometries were investigated to study the main differences between one solution and the others. The results showed that no important improvements in terms of combustion efficiency were obtained by using the new piston bowl shapes, which was mainly due to the very low (+4%) or null increase in turbulent kinetic energy during the compression stroke and due to the higher heat losses (+20%) associated with the increased surface area of the new piston geometries.

Keywords: premixed turbulent combustion; light-duty engine; natural gas; FAM; CFD; RANS

1. Introduction

Nowadays, the study and development of alternative fuels are gaining more and more interest as one of the possible solutions for reducing greenhouse gas and pollutant emissions [1,2]. Different gaseous fuels, such as natural gas, shale gas, and hydrogen, are currently being investigated in order to avoid the formation of particulate matter [3–5]. In the truck sector, diesel fuel can be substituted with natural gas due to the different advantages offered by this fuel; the high H/C ratio leads to a reduction in CO_2 emissions with respect to other fuels, and the opportunity to use lean mixtures reduces the nitrogen oxide emissions and improves the thermal efficiency. Furthermore, the conversion costs associated with the modification of existing diesel-fueled engines into spark-assisted natural-gas-fueled engines are relatively low. Through the use of a simplified after-treatment system, this approach is widely used in light- and heavy-duty engines to meet emission standards [6,7]. On the other hand, natural gas presents an important drawback related to its low power density. To this end, different solutions have been investigated over the years, including direct injection systems, lean combustion coupled with an advanced ignition system, and dual-fuel operation [8–13].

Within this context, the study and understanding of all processes that take place inside a combustion chamber become fundamental for achieving high efficiencies and low pollutant emissions. In light-duty engines, the thermodynamic conditions encountered in the combustion chamber are quite different from those found in passenger car engines; higher pressures and temperatures are expected due to the use of turbocharging and high compression ratios [14]. Moreover, since most natural gas engines are derived from compression-ignition ones, the intake system is designed to generate a swirling motion inside the combustion chamber, even if tumbling is more desirable for turbulence generation during the compression stroke. For this reason, different piston bowl geometries [15–17] and new combustion chamber layouts [8,18] are currently being examined.

To support engine design, CFD has become a powerful and efficient tool for studying the combustion process, from ignition to the burn-out phase. Over the years, different combustion models have been proposed, and the main challenges were expressed according to the correct description of the ignition stage, the laminar-to-turbulent flame transition, and suitable prediction of the flame wrinkling in different regimes to correctly model fully turbulent combustion. The main parameters that can be used to identify these flame conditions are the laminar flame speed S_u, the turbulence intensity u', the turbulence integral length L_t, and the flame thickness δ_f [19].

The most commonly used combustion models found in the literature are the coherent flamelet model (CFM) and the *G*-equation. The former is based on transport equations for c, the combustion progress variable, and Σ, the flame surface density [20,21], whereas the latter solves a transport equation for the non-reacting scalar G, thus bypassing the need for a source-term closure and the problems associated with counter-gradient diffusion [19,22–24]. The use of these models for the simulation of spark-ignition engines has been successfully validated over the years [23,25–28] by using simplified or more detailed ignition models [29,30] and both RANS and LES models for turbulence [25,31]. However, depending on their applications, different versions of the CFM have been proposed in the literature. When using this approach, the reaction rate tends to have an "Eddy-Breakup"-like expression under equilibrium conditions [32]; thus, it fails to reproduce the flame behavior near walls in complex flows and large geometries [33]. Furthermore, the need to tune at least two model constants without a general agreement on the formulations to use for flame surface density production and destruction terms [34] strongly affects the predictive capability of this approach. Regarding the *G*-equation model, its implementation in CFD code is not straightforward due to the different definitions of the *G* field, and appropriate constraints should be used to guarantee geometrical consistency and avoid numerical instabilities [35].

The main scope of this work is the development and validation of a multi-dimensional model to predict combustion in spark-ignition natural gas engines. The one-equation flame area model (FAM) proposed by Weller was used for this purpose due to its ability to describe the main combustion phases with a limited number of tuning constants. This model solves the transport equation of the combustion regress variable b, while an algebraic expression of the flame wrinkling factor Ξ is used for the reaction rate. The main advantages with respect to the CFM and the G-equation model are the choice of a regress variable that ensures numerical stability and the possibility of taking suitable expressions for Ξ from the literature [19,36]. Ignition is described through a deposition model, whereas the laminar-to-turbulent transition is considered by means of a semi-empirical model derived from the work of Herweg and Maly [37]. Simulations were carried out by using the Lib-ICE code developed by the ICE Group of Politecnico di Milano. Lib-ICE is based on the OpenFOAM software, and it was successfully applied by the authors for the simulation of IC engines in previous works [8,38–42].

The proposed approach was validated by using experimental data from a modern light-duty SI natural gas engine. First, three different operating conditions were simulated at various engine speeds and loads with the original piston bowl shape. The computed results were compared with experimental data on the in-cylinder pressure, heat release rate, and

pollutant emissions (*NO* and *CO*). Then, the model was applied to study two other piston bowl geometries that were manufactured and tested to try to improve the combustion efficiency. Experimental validation was carried out by comparing the computed and experimental data on the in-cylinder pressure, heat release rate, and pollutant emissions. The simulations allowed us to understand the effects of piston bowl geometry on the combustion process.

2. Numerical Models

In this section, the main aspects related to the computational models used are presented. First, an overview of the mesh management for the gas exchange and the combustion phases is given. Then, the combustion model developed in this work on the basis of the one-equation Weller approach is described. In particular, all sub-models used to represent the flame from ignition to the turbulent combustion stage, together with the strategies adopted to predict the laminar flame speed and composition of the burnt mixture, are reported in detail.

The governing equations were solved by using a RANS approach in order to speed up the computational time, and the $k - \epsilon$ model was used for turbulence with the standard coefficients suggested in the literature.

During the simulations, two different approaches were used to manage the mesh during the gas exchange and combustion process:

1. Exhaust and intake phases: Multiple deforming grids were used to accommodate the motion of the piston and valves [40];
2. Compression and combustion phases: Dynamic mesh layering was employed. Layers of cells were added or removed above the piston surface during its motion [43,44].

At the end of gas exchange simulations, the flow field at the IVC was mapped onto the grid used for the combustion simulation.

2.1. Flame Area Model

The proposed combustion model was founded on the one-equation flame area model described in Weller's work [33]. Based on the laminar flamelet assumption, it describes a flame's development through the regress variable b and the flame wrinkling factor Ξ. The former represents the unburned gas fraction, so it is equal to 1 in the fresh mixture and 0 when the charge is completely burned. The regress variable's transport equation is, therefore, described by:

$$\frac{\partial \rho \tilde{b}}{\partial t} + \nabla \cdot \left(\rho \tilde{\mathbf{U}} \tilde{b} \right) - \nabla \cdot \left(\mu_t \nabla \tilde{b} \right) = \rho_u \, \tilde{S}_u \, \tilde{\Xi} \, |\nabla \tilde{b}| + \dot{\omega}_{ign} \tag{1}$$

where ρ and ρ_u are the density of the mixture and unburned mixture, respectively, μ_t is the turbulent viscosity, and S_u is the unstrained laminar flame speed. The contribution of the ignition process is represented by $\dot{\omega}_{ign}$, while the first term on the RHS is the reaction rate due to turbulent flame propagation. The term Ξ is the flame wrinkling factor, and it is defined as the ratio between the turbulent and the unstrained laminar flame speed S_t / S_u. The relation between the flame wrinkling factor and flame surface density Σ is described by:

$$\Sigma = \Xi \, |\nabla \tilde{b}| \tag{2}$$

One of the advantages of using Weller's formulation is that Equation (1) can be solved fully implicitly by exploiting differential operator properties. This ensures numerical stability and independence from the time step, both of which are very important when real geometries with complex grids are used.

2.2. Ignition Model

An initial distribution of the regress variable is required to start the flame propagation process. This task is carried out with a simplified deposition model, such as the one

used in [45], whereas more complex approaches validated by other authors [28,46] will be integrated into future work. Starting from a user-defined initial flame kernel diameter d_{ign} and time interval Δt_{ign}, an ignition source term is imposed in the transport equation in the cells for which the distance from the spark plug is less than $r_{ign} = d_{ign}/2$:

$$\dot{\omega}_{ign} = \frac{C_s \, \rho_u \, b}{\Delta t_{ign}} \tag{3}$$

where C_s is a user-defined coefficient, ρ_u is the unburned gas density, and Δt_{ign} is the ignition duration specified by the user.

2.3. Turbulent Combustion Model

Once the regress variable is initialized by the ignition model and the flame propagation process is started, a suitable expression for the flame wrinkling factor Ξ that allows the flame front to develop from its initial laminar state to a fully turbulent flame is required, as shown in the first RHS term of Equation (1). In this work, Ξ is modeled according to authors' previous work [41].

The expression for the flame wrinkling factor under the equilibrium condition Ξ_{eq}^* is taken from the Peters formulation [19]:

$$\Xi_{eq}^* = 1 - \frac{a_4 b_3^2}{2b_1} \frac{L_t}{\delta_{th}} + \left[\left(\frac{a_4 b_3^2}{2b_1} \frac{L_t}{\delta_{th}} \right)^2 + a_4 b_3^2 \frac{u' L_t}{S_u \delta_{th}} \right] \tag{4}$$

where δ_{th} is the flame thickness, and it is defined as:

$$\delta_{th} = \frac{(\lambda / c_p)_u}{\rho_u S_u} \tag{5}$$

Here, δ is the heat conductivity, c_p is the heat capacity, and ρ_u is the density, all of which are evaluated in the unburned gas. The values of the constants a_4, b_1, and b_3 are reported in Table 1.

Table 1. Constants used for the correlation of the equilibrium wrinkling factor.

Constant	Suggested Value	Origin
a_4	0.78	$D_t = \nu_t / 0.7$
b_1	2.0	Experimental data
b_3	1.0	Damköler (1940)

2.4. Laminar Flame Speed Correlation

Laminar flame speeds are read from a lookup table in which the S_u values are stored as a function of the unburned temperatures, pressures, equivalence ratios, and EGR. This table is generated by a one-dimensional laminar flame speed solver operating under constant-pressure conditions. The fuel was assumed to be pure methane and the GRI mechanism was used in the calculation [47].

2.5. Species Calculation

The chemical composition in each cell is calculated while knowing the mass fraction of the chemical species in the burned $Y_{b,i}$ and unburned $Y_{u,i}$ states and the regress variable b:

$$Y_i = b \cdot Y_{u,i} + (1 - b) \cdot Y_{b,i} \tag{6}$$

Burned gas chemical composition $Y_{b,i}$ is computed in this work with two different methodologies. The first one is based on tabulated kinetics, and the approach was described in detail in [48]. The chemical compositions and reaction rates are stored in a lookup table that is generated through constant-pressure homogeneous reactor calculations at different

values of pressure, equivalence ratios, and unburned gas temperatures. To access the lookup table, the unburned gas enthalpy h_u transport equation is solved, which provides the temperature of the fresh charge T_u. Differently, the burned gas enthalpy h_b is computed from h_u, the mean cell value h, and the regress variable:

$$h_b = \frac{h - b \cdot h_u}{1 - b} \tag{7}$$

Accordingly, the burned gas temperature T_b is computed from h_b and the composition $Y_{i,b}$.

The second approach is based on chemical equilibrium according to [49]. The burned gas chemical composition $Y_{b,i}$ is, therefore, calculated at each time step with an iteration scheme, and the chemical system is composed of four elements (C, H, O, N) and ten reacting species (H_2O, CO_2, CO, O_2, H_2, N_2, H, O, OH, NO).

3. Experimental Setup

The experimental setup was composed of a Schenck Dynas bench with a Horiba STARS automation system, as shown in Figure 1. The natural gas fuel was composed, on average, of 94.5% methane on a molar basis, with small variations among the different CNG bottles. Then, the remaining molar shares consisted of ethane (3.5%), higher hydrocarbons and hydrogen (0.7%), and inert gases (1.3%), such as nitrogen and carbon dioxide. The fuel mass flow rate was measured by using a Rheonik RHM 015 GNT Coriolis-type flow meter with an associated uncertainty of 0.2%.
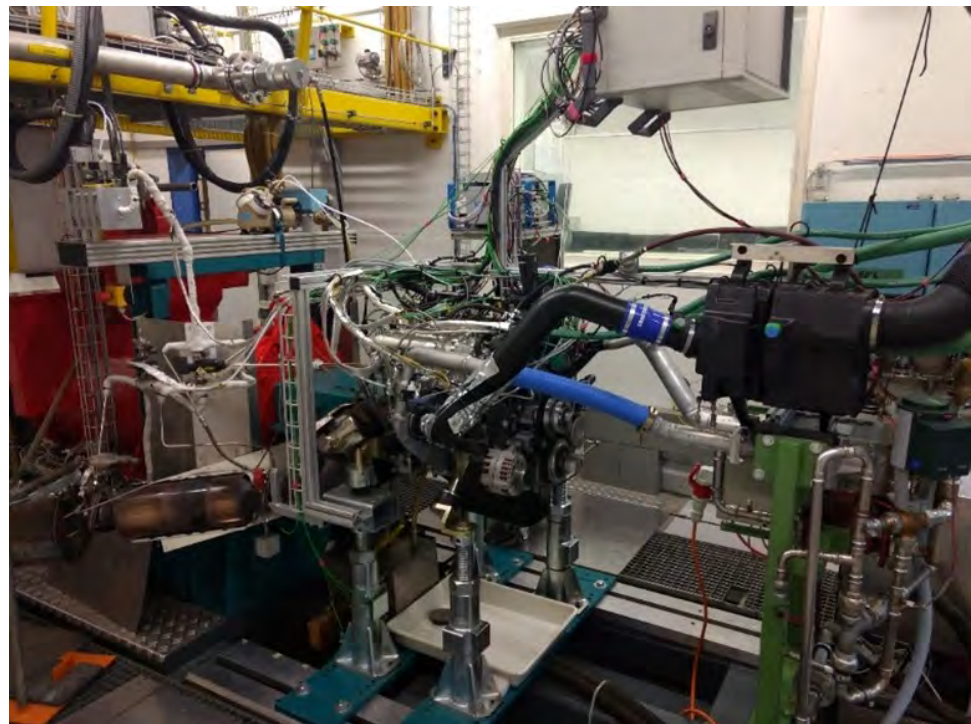

Figure 1. Test bench facility.

All tests were performed by using conditioned air at 24 °C and 60% relative humidity. The air mass flow rate was measured by using a hot-film anemometer (ABB Sensyflow FMT700-P) with an associated uncertainty of 1%. Figure 2 presents the scheme of the test bench and its major measurement devices.
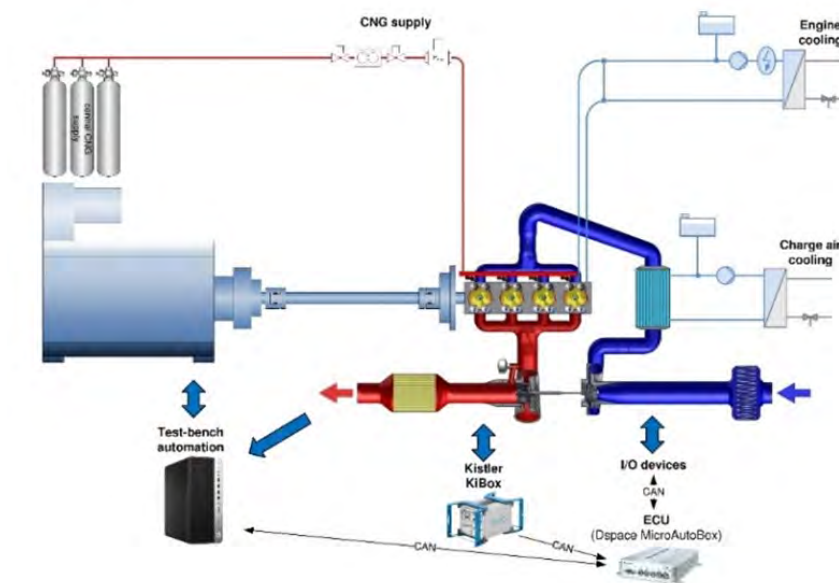
Figure 2. Test bench scheme.

The experimental data were measured by using two different systems:

- Crank-angle-based data were collected by using a Kistler Kibox triggered by a Kistler 2614A1 crank-angle sensor. Moreover, cylinder 1 was equipped with a piezoresistive Kistler 4007B sensor in the intake manifold and a water-cooled piezoresistive Kistler 4049B10 sensor in the exhaust manifold. The Kistler Kibox was used to control the spark timing and the knock index derived from the cylinder pressure.
- Time-based information, such as pressure, temperature, mass flows, feedback signals from actuators, and data from the exhaust gas analyzer, were recorded by the test bench automation system. An anti-aliasing filter was used on each analog channel, and a frequency of 1 Hz was used to record 60 s of measuring time.

Figure 3 shows the scheme of all of the pressure, temperature, and lambda sensors mounted on the engine.
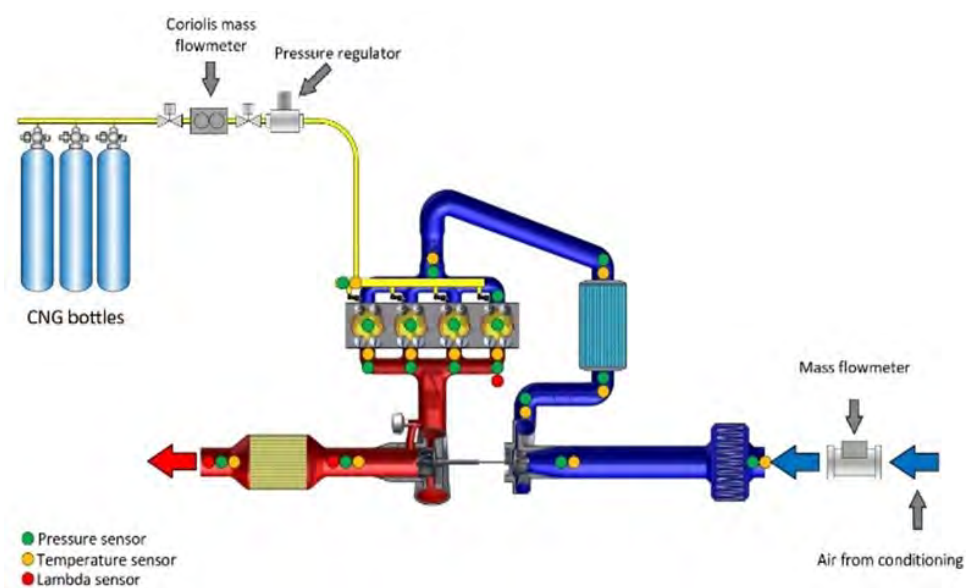

Figure 3. Sensor placement scheme.

4. Simulated Conditions

To validate the proposed methodology for the simulation of the combustion process in an SI engine fueled with natural gas, full-cycle simulations of a four-cylinder turbocharged engine—whose main geometric data are reported in Table 2—were performed. In particular, three different piston bowl geometries were studied on Empa test benches; the original piston was compared with two other geometries that, from preliminary considerations, should have given an increase in turbulence inside the combustion chamber and, thus, improved the combustion process. A star shaped piston was selected according to the work of Wohlgemuth et al. [17], where a similar piston bowl geometry was investigated with the aim of improving the turbulence inside the combustion chamber at TDC. In particular, a star-like shape was chosen to disrupt the swirl charge motion due to the inner edges and to transform it into turbulence. The number of leaves was chosen as a compromise between a rugged geometry and higher heat losses. According to Wohlgemuth's work, the modified piston bowl geometry was able to increase the turbulent kinetic energy at TDC by up to 100%. The tower piston was inspired by the activity of Heuser et al. [16], where a geometry characterized by squish areas with cutout sections was considered, with the aim of converting the swirl motion into turbulent kinetic energy inside the combustion chamber. The results presented by Heuser showed that the mean turbulent kinetic energy was not highly affected by the proposed piston bowl geometry, whereas a zone of higher turbulence was found in the area underneath the combustion chamber's ceiling, which was particularly relevant for early flame development. Figure 4 illustrates the details of the three different piston bowl geometries.

Table 2. Main engine geometry data of the simulated SI engine.

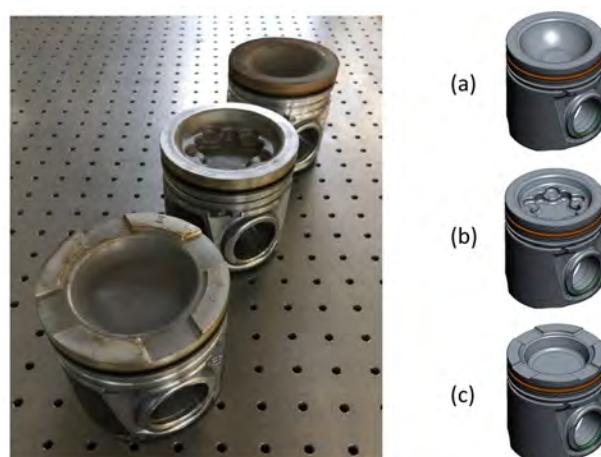|	
Bore	95.8 mm
Stroke	104 mm
Connecting rod	160 mm
Displaced volume	3.0 L
Compression ratio	14.5
Number of valves	4
IVO	−171 deg ATDC
EVO	110 deg ATDC

Figure 4. Different piston bowl geometries that were manufactured (**left**) and those from the software program (**right**): original piston (**a**), star piston (**b**), and tower piston (**c**).

Three different operating conditions were investigated, as reported in Table 3: one low-load point running at 1000 rpm, one medium-load point running at 2200 rpm, and one full-load point running at 3500 rpm. These operating conditions were chosen in order

to validate the proposed methodology under considerably different conditions without changing the model constants.

Table 3. Details of the simulated operating conditions of the light-duty natural gas engine.

Condition	A40	B50	C100
Speed [rpm]	1000	2200	3500
Torque [Nm]	125	200	275
Lambda	1	1	1

First, simulations of the gas exchange process were performed—starting from EVO and going until IVC—to study the effect of the piston bowl shape on the turbulence distribution during the intake process. The average in-cylinder cell size was 1.5 mm, and, during the gas exchange process, the total number of computational cells ranged from 1.5 to 1.7 million, depending on the piston bowl geometry considered (Figure 5). The number of meshes required for one simulation varied from 80 to 90 depending on the piston bowl geometry and the operating conditions considered. Simulations were carried out on a 24-core machine (Intel(R) Xeon(R) CPU E5-2690 v4 processor with 2.60 GHz), and the CPU time varied from a minimum of 18 hours to a maximum of 2 days, depending on the operating conditions and on the considered mesh.
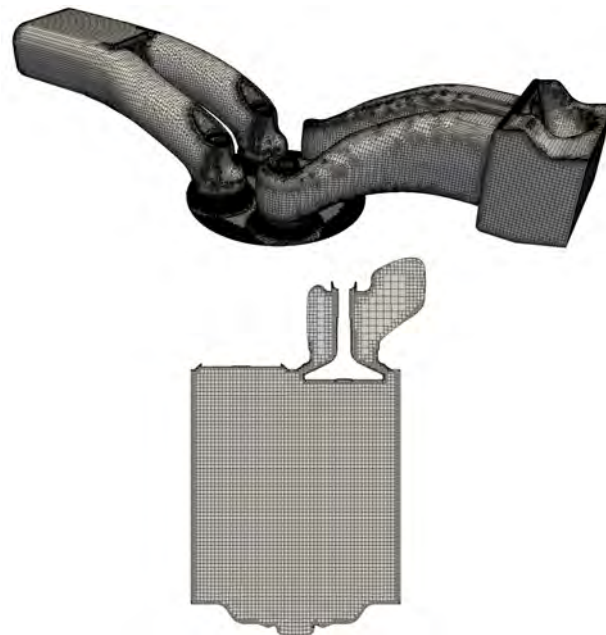

Figure 5. Example of the grid used for the cold flow simulation: full view of the mesh during the overlap phase (**top**) and cross-section of the grid during the intake phase (**bottom**).

Figure 6 shows the computational grid used for the combustion simulations, whereas Table 4 reports the main mesh information. Because the natural gas injection was not taken into consideration during the gas exchange phase, a uniform distribution of natural gas was imposed in the combustion mesh under stoichiometric conditions.

Table 4. Combustion mesh information.

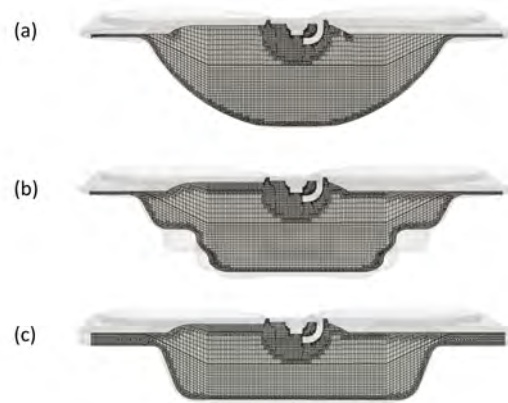|	
Mean cell size	0.5 mm
Spark plug zone cell size	0.25 mm
Maximum number of cells	~2 million
Minimum number of cells	~435,000

Figure 6. Computational meshes used for combustion simulations: original piston (**a**), star piston (**b**), and tower piston (**c**).

5. Results and Discussion

5.1. Experimental Results

The experimental investigation conducted by Empa Automotive Powertrain Technologies on the new piston bowl geometries (star and piston) showed that no important improvements in terms of combustion duration were achieved. As shown in Figure 7, where the different combustion durations in terms of CA10-90 are reported, the tower and star pistons always presented a longer combustion compared to that of the original piston, except for the medium-load condition, where the combustion durations of the star and original pistons were similar.

Within this context, the CFD methodology proposed in this work was used to better understand why the new geometries were not able to improve the combustion efficiency as expected.
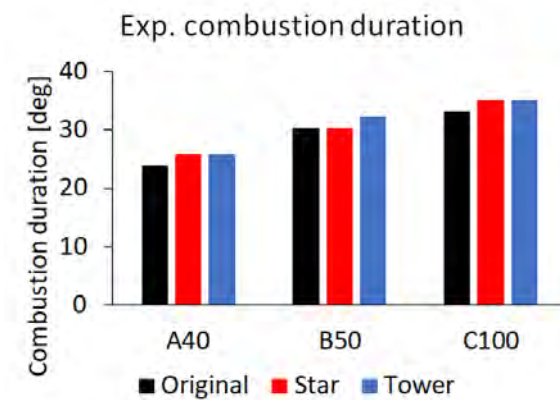

Figure 7. Comparison of the experimental combustion durations for the three operating points when using the three different piston bowls.

5.2. Cold Flow Simulation

Cold flow simulations of the gas exchange processes were performed for the following purposes:

1. To compare results in terms of turbulence intensity inside the combustion chamber, since the main scope of these geometries was to convert the swirl motion into turbulence inside the combustion chamber;
2. To have information about the flow field for the combustion simulations.

In Figure 8a, the fluctuating component u' is plotted as a function of the crank angle for the low-load condition; the star piston was able to increase the turbulence inside the

combustion chamber by a small amount (+5%), whereas no important differences were visible between the original and tower piston bowls.

Moving to the medium-load condition, the influence of the piston geometry on the turbulence was similar to that with the low-load operating point, as shown in Figure 8b. The star piston bowl was capable of increasing the turbulence by a small amount (+4%) with respect to the original geometry, whereas the tower piston, in this condition, produced an even lower turbulence than that of the original geometry. Figure 9 reports the turbulent kinetic energy distribution on a plane orthogonal to the cylinder axis placed 5 mm below the cylinder head for the three investigated piston geometries. It is clear that the star piston bowl was capable of spreading the region of relatively high turbulence (orange color) close to spark plug more than the other two investigated pistons were.
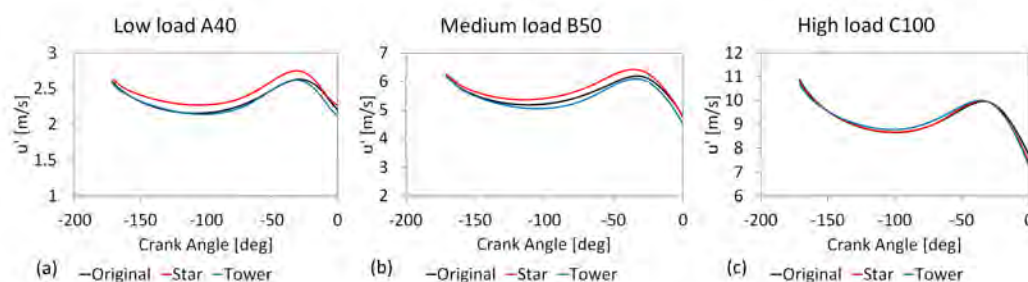

Figure 8. Turbulence intensity evolution inside the combustion chamber for the three different piston bowl geometries under low-load (**a**), medium-load (**b**), and high-load (**c**) conditions.

Finally, the high-load condition was investigated, and the results in terms of turbulence intensity are reported in Figure 8c. The three different piston bowls generated the same amount of turbulence inside the combustion chamber, and so no important differences in combustion duration were expected.

From this analysis, a very limited increase in turbulence was calculated by using the new piston geometries for the investigated conditions, and this could be one of the reasons for why no improvements in combustion duration were experimentally observed. Looking at the results presented by Wohlgemuth [17], it seems that most of the work in converting swirl motions into turbulence was done before the IVC, and only a small portion occurred during the compression stroke. On the other hand, looking at Figure 8, it is clear that, at the beginning of the compression stroke, the turbulence was almost identical for all three piston bowl geometries. This difference could be explained by the different intake systems used in the two engines. It is worth mentioning that the engine used in Wohlgemuth's work had only one intake valve and a quite different bore-to-stroke ratio (1.23) than that used in this work (0.92).
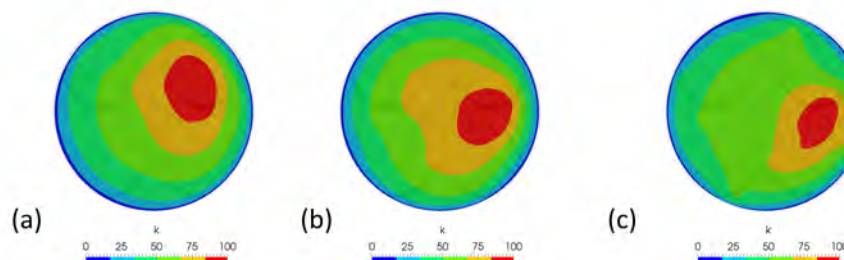

Figure 9. Kinetic energy distribution of turbulence on a plane orthogonal to the cylinder axis placed 5 mm below the cylinder head flow for the original (**a**), star (**b**), and tower (**c**) piston bowls.

5.3. Validation of the Combustion Model on the Original Piston Bowl

The proposed methodology was then validated by using the experimental results of the operating condition named B50 with the original piston bowl. The combustion model's tuning constants are reported in Table 5. The b_1 constant used in Equation (4) to compute the equilibrium wrinkling factor was slightly reduced with respect to that suggested in the literature to obtain a better match with the experimental data. Even though the ignition phase was modeled with a simple deposition model here, the tuning of the ignition constants is fundamental for generating a stable kernel and, thus, for allowing the correct propagation of the flame in the combustion chamber. To do that, a relatively small value of d_{ign} had to be coupled with a high value of C_s to avoid any significant influence of the ignition model on the heat release profile. Moreover, different values of Δt_{ign} were used in order to keep the same duration in milliseconds, depending on the rotational speed. Nevertheless, the same intensity for ignition was used by keeping the ratio $\frac{C_s}{\Delta t_{ign}}$ constant. Simulations were carried out by using the same machine that was mentioned above, and the CPU time was about 24 h for the conditions simulated with chemical equilibrium and 12 h for those run with tabulated kinetics.

Table 5. Combustion model's tuning constants for the different operating conditions. Δt_{ign} and t_{spk} are in degrees.

Condition	C_s	Δt_{ign}	b_1	C_{vol}	C_{Tay}	t_{spk}
A40	2	3	1.8	10	1	−14.6
B50	4.4	6.6	1.8	10	1	−25.5
C100	7	10.5	1.8	10	1	−21.8

Figure 10a reports a comparison between the computed and experimental values of the in-cylinder pressure and apparent heat release rate (AHRR) profiles for the medium-load condition. The pressure peak location and amplitude were correctly estimated by the combustion model. Looking at the AHRR curve, a good estimation of the ignition, transition, and fully turbulent phases was achieved.

Figure 10b shows the results of the full-load operating condition when running at 3500 rpm. Here, the peak pressure location was, again, correctly estimated, but with an underestimation of the maximum amplitude. This behavior was caused by a turbulent combustion rate that was slightly lower than the experimental value, as shown by the AHRR profile.

Finally, the low-load operating condition (A40) was simulated. The results in terms of the in-cylinder pressure and apparent heat release are reported in Figure 10c. The peak pressure location was correctly predicted, whereas an overestimation of the absolute value was observed. This behavior could be attributed to an overestimation of the trapped mass inside the combustion chamber, since the computed in-cylinder pressure was already above the experimental value at −20 CAD ATDC—before the advance of the and, thus, before the start of combustion. Moreover, looking at the apparent heat release profile, the ignition, laminar-to-turbulent transition, and fully turbulent combustion rate were in good agreement with the experimental data until the AHRR peak. After the peak, the computed AHRR curve was always above the experimental one, meaning that a higher mass burned during the combustion process.
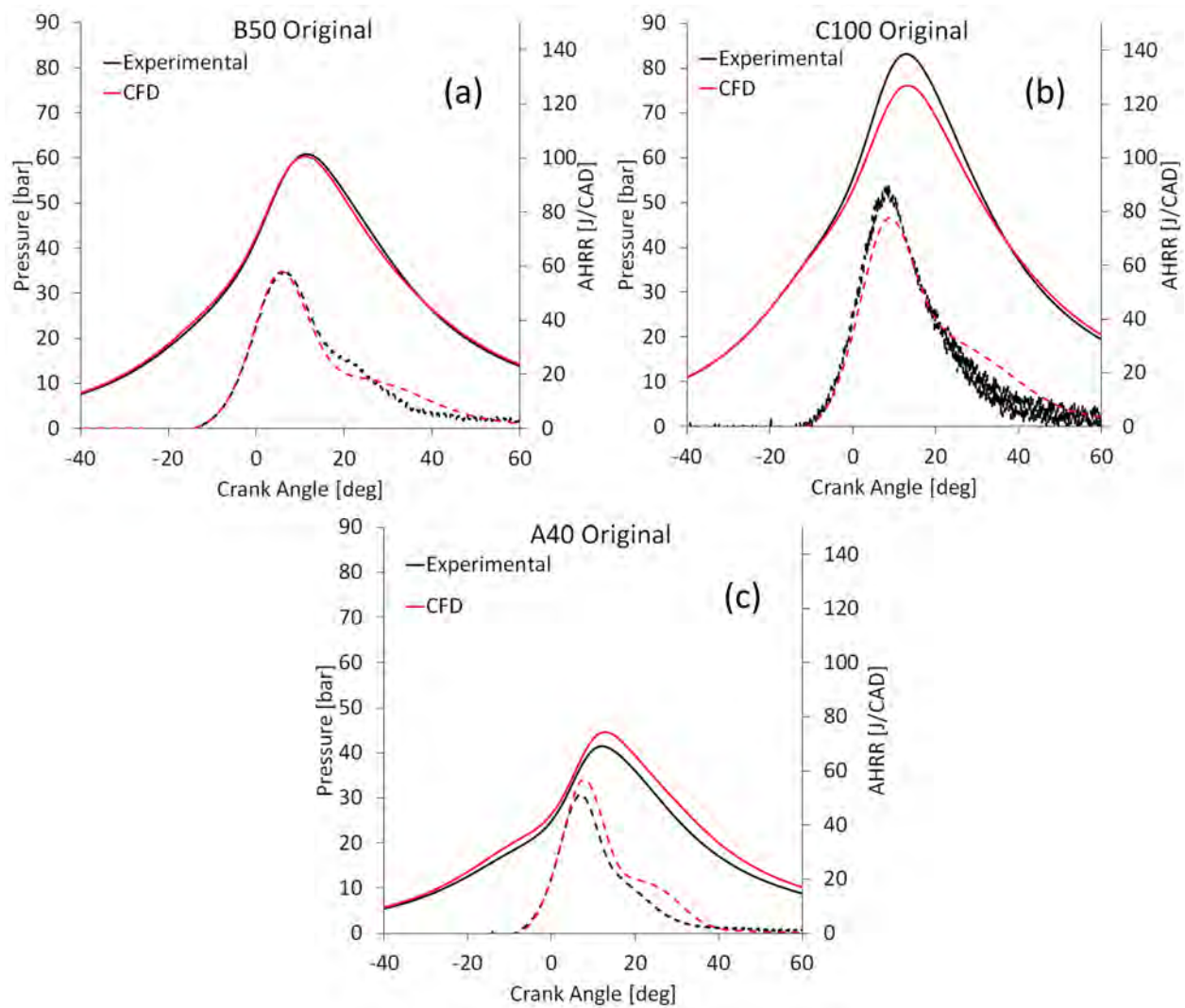
Figure 10. Comparison between the computed and experimental data of the in-cylinder pressure (solid lines) and apparent heat release rate (dashed lines) for the medium-load (**a**), high-load (**b**), and low-load (**c**) conditions when using the original piston.

5.4. Combustion Model Validation Using Different Piston Bowl Shapes

After the assessment of the combustion model with the original piston, the other two piston bowl shapes were investigated in order to analyze the influences of different geometries on the combustion performance.

First, the medium-load point (B50) was simulated by using the star piston bowl, and the results are reported in Figure 11a. The peak pressure location was, again, correctly predicted, meaning that ignition and transition phases were well described by the combustion model. However, the maximum pressure was slightly overestimated, since the turbulent combustion rate was higher than the experimental one, as can be seen from the AHRR profile. This discrepancy could have been caused by the higher turbulence predicted by the CFD solver for the star piston, which can also be seen in all of the investigated operating conditions.

Figure 11b reports the results for the tower piston bowl shape. As for the original piston, the pressure and heat release traces were in good agreement with the experimental data.
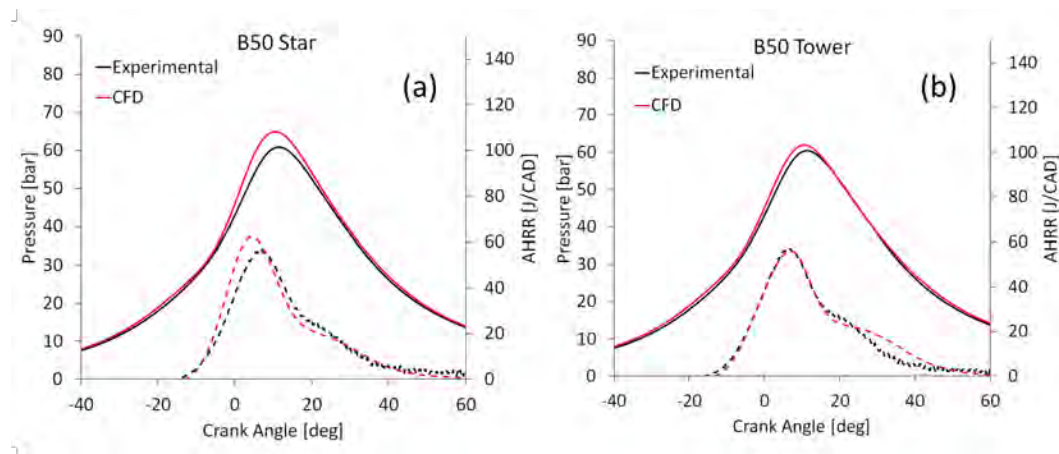
Figure 11. Comparison between the computed and experimental data of the in-cylinder pressure (solid lines) and apparent heat release rate (dashed lines) for the B50 operating point when using the star (**a**) and tower (**b**) pistons.

To gain a better understanding of the geometrical influence on combustion, Figure 12 shows the variations in the combustion duration when using the three different piston bowl shapes, computed as the crank angles needed to burn the charge from 10% to 90%. Experimentally, the star piston presented the same combustion duration as that of the original one, whereas in the simulation, faster combustion was predicted, as shown previously. The tower shape led to a longer combustion—around 2 CAD—which was correctly estimated with CFD. This behavior can be seen also in Figure 13, where the flame's development from the side and the top views of the combustion chamber is reported for the three different piston bowls. On top of each sub-figure, the temperature field is visualized on a plane positioned in the middle of the combustion chamber while passing through the spark plug. On the bottom, instead, the flame is represented as a $b = 0.5$ iso-surface. At -10 CAD ATDC, the tower piston showed a more developed flame due to the slightly anticipated spark timing. At TDC, the star piston presented a larger flame front due to the higher turbulence intensity, indicating faster combustion in this angle range. At 15 CAD ATDC, the three flames looked similar, even though the star bowl was the one that had slightly more mass that was burned at this crank angle.
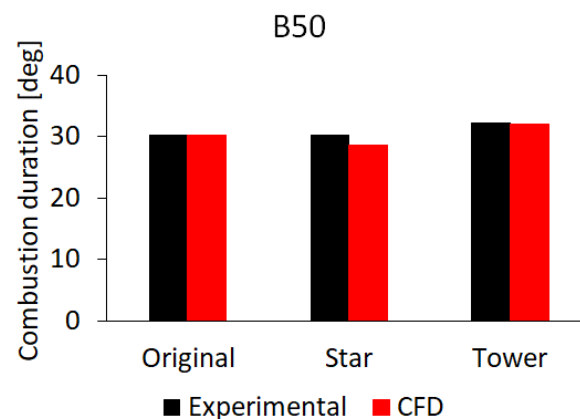

Figure 12. Comparison between the computed and experimental combustion durations for the B50 operating point and the three different piston bowls.
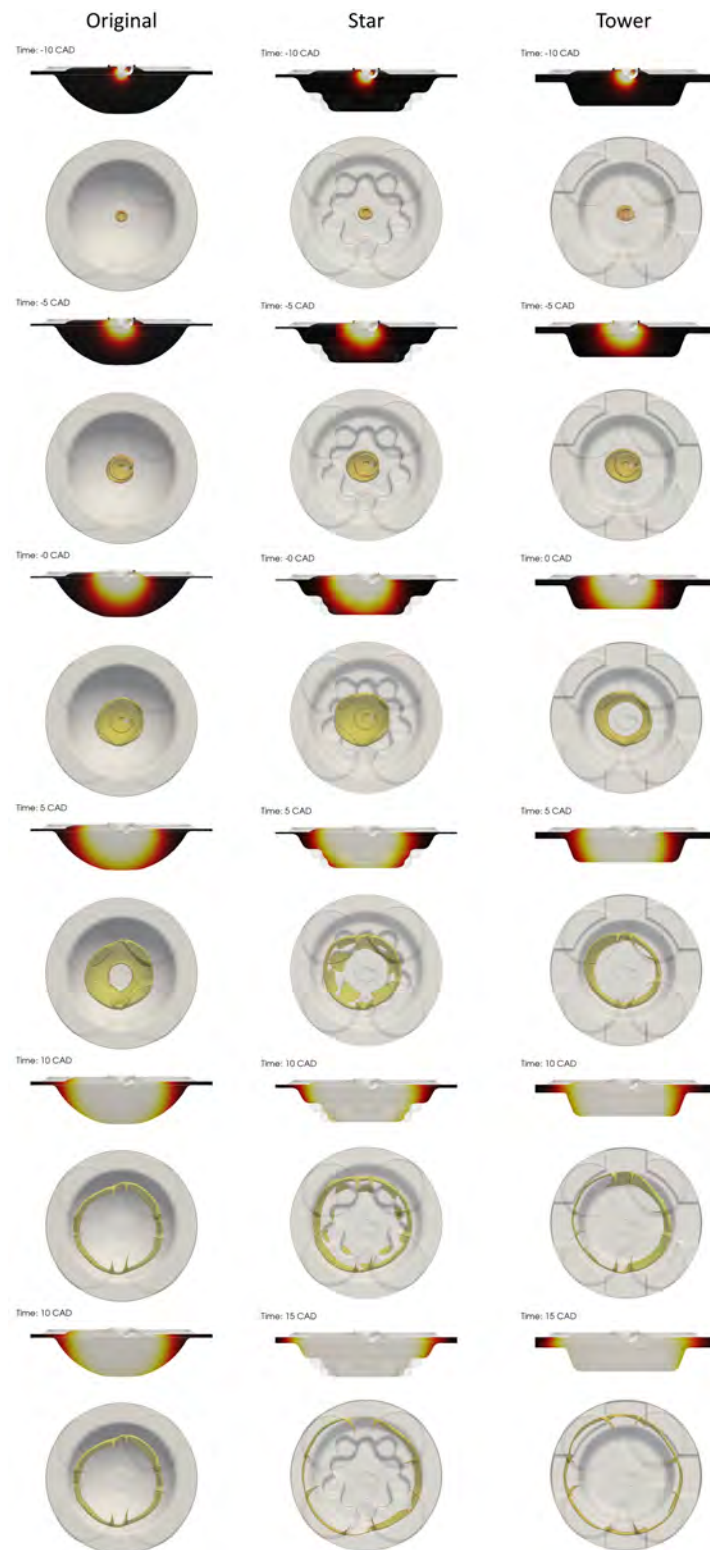
Figure 13. Flame propagation process for the B50 operating condition when using the three different piston bowl geometries. On top of each sub-figure, the temperature field is visualized on a plane passing through the spark plug's center. On the bottom of each sub-figure, an iso-surface with $b = 0.5$ is reported.

Moving to the full-load operating point, the CFD results in terms of pressure and heat release rate for the star piston were in good agreement with the experimental values,

as shown in Figure 14a. All of the principal phases, from ignition to fully turbulent combustion, were well described by the combustion model.
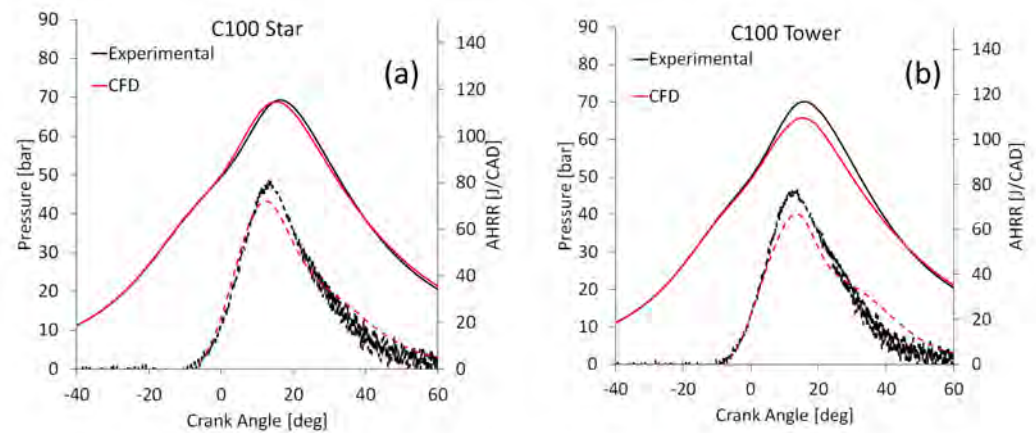

Figure 14. Comparison between the computed and experimental data of the in-cylinder pressure (solid lines) and apparent heat release rate (dashed lines) for the C100 operating point when using the star (**a**) and tower (**b**) pistons.

When using the tower bowl shape, a small underestimation of the pressure peak can be observed in Figure 14b, even though the combustion phase was well predicted, as shown by the peak pressure position. This discrepancy can be explained, as for the original piston, by the small underestimation of the fully turbulent combustion rate.

The proposed combustion model was capable of correctly predicting the slower burning rates of the star and tower piston bowls with respect to the original one, as shown in Figure 15. CFD overestimated the combustion duration by one CAD for the star bowl and by two CADs for the tower bowl, but a rather satisfactory result was achieved.
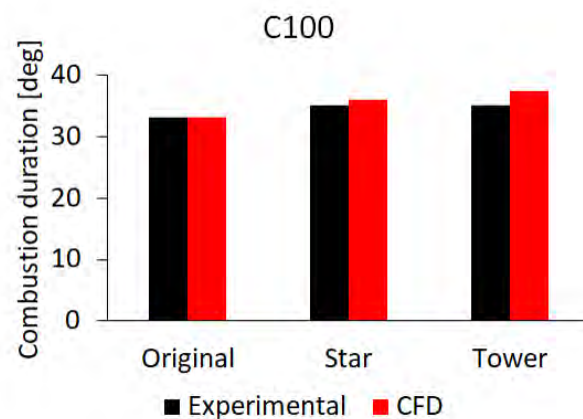

Figure 15. Comparison between the computed and experimental combustion durations for the C100 operating point and the three different piston bowls.

Finally, the low-load condition (A40) was simulated by using the modified geometries and compared with the experimental data. Again, the star piston presented a higher combustion rate than expected due to the high turbulence generated in the combustion chamber. As a consequence, the peak pressure was overestimated, as shown in Figure 16a, and this phenomenon was also amplified by the larger mass trapped in IVC.
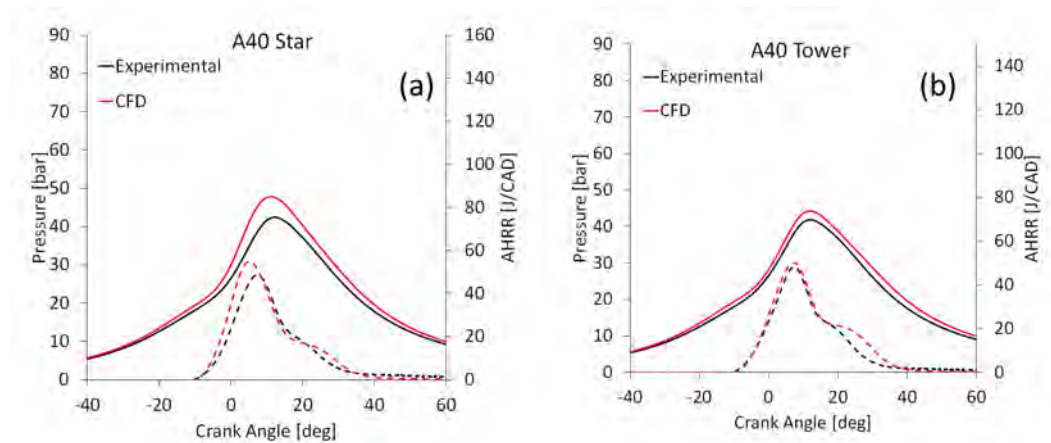
Figure 16. Comparison between the computed and experimental data of the in-cylinder pressure (solid lines) and apparent heat release rate (dashed lines) for the A40 operating point when using the star (**a**) and tower (**b**) pistons.

Figure 16b reports the main results for the A40 operating condition when using the tower piston bowl. The apparent heat release rate accurately matched the experimental profile, and the combustion phasing was well predicted, as shown by the correct peak pressure location. The higher maximum pressure was justified again by the overestimation of the trapped mass in IVC, as can be seen from the difference in pressure traces before the spark's advance.

Figure 17, which reports a comparison between the computed and experimental combustion durations when using the different piston bowls, shows that, for the tower geometry, the longer combustion was correctly predicted. However, the CFD simulation using the star piston bowl predicted a faster combustion than that obtained when using the original piston. This behavior, which was not verified experimentally, was probably the consequence of the higher turbulence predicted in the combustion chamber, which led to faster combustion.
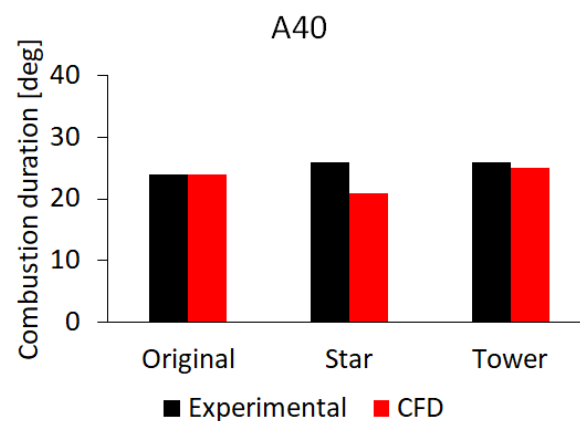

Figure 17. Comparison between the computed and experimental combustion durations for the A40 operating point and the three different piston bowls.

To complete the analysis, in Figure 18, the crank angles needed to burn the first 10% of the total fuel mass—namely, CA 0-10—are shown, since this phase is crucial for the cyclic variations [50]. A rather fast flame development was observed for the A40 operating condition, which indicated a lower possibility of cyclic variations, and by using the tower piston geometry, it was possible to further reduce the combustion duration by two CADs. No important effects of the piston bowl geometry were observed for the other two conditions analyzed.
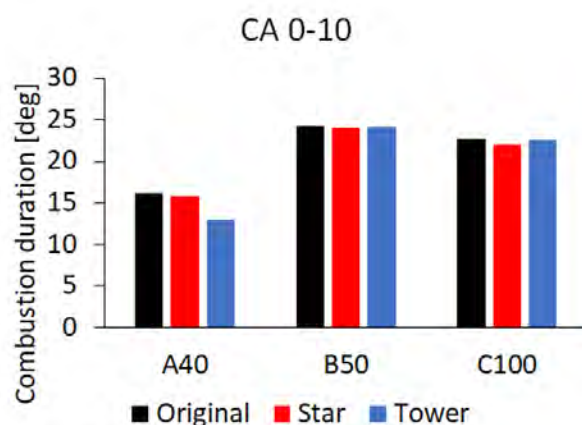
Figure 18. Comparison of the simulated combustion durations in terms of CA 0-10 for the analyzed operating conditions and the three different piston bowls.

Another important aspect that can affect the combustion efficiency is the heat transferred through the walls and, in particular, through the piston. As shown in Figure 19, in which the computed heat transfer through the piston is reported as a function of the crank angle for the medium-load condition, the new geometries presented higher heat losses due to the increased surface area exposed to combustion. The combination of higher heat losses with the very low increase in turbulence during the intake stroke is probably the main reason for why no improvements in combustion efficiency were experimentally observed.
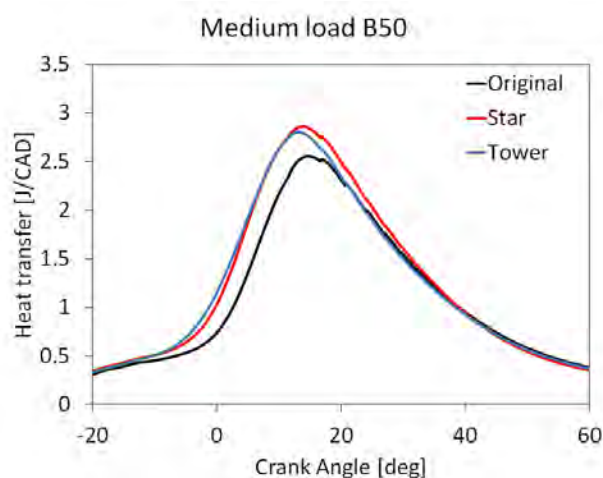

Figure 19. Simulated evolution of heat transfer through the piston for the three different investigated geometries at a medium load.

5.5. Pollutant Emissions

After the validation of main thermodynamic parameters, an analysis of pollutant emissions was performed. First, the final *NO* emissions were compared with the experimental data, as shown in Figure 20. The results are normalized by the value obtained by using the original piston in order to gain a better understanding of the advantages of changing the piston bowl shape. Moreover, the results obtained by using chemical equilibrium and tabulated kinetics are reported in the graph. Experimentally, there were no significant differences in *NO* emissions by changing piston geometry for the A40 and B50 operating points—this was correctly predicted by the CFD simulations with a small error margin—and, in particular, by using chemical equilibrium for the species calculation. Nevertheless, a 20% reduction was obtained by using the modified geometries for the full-load operating condition. Again, the proposed methodology was capable of predicting

this reduction in *NO* emissions with an error margin of approximately 10% for chemical equilibrium. The tabulated kinetics were able to better estimate the effect of changing the geometry, but when using chemical equilibrium, the absolute final values of *NO* emissions were closer to the experimental ones.
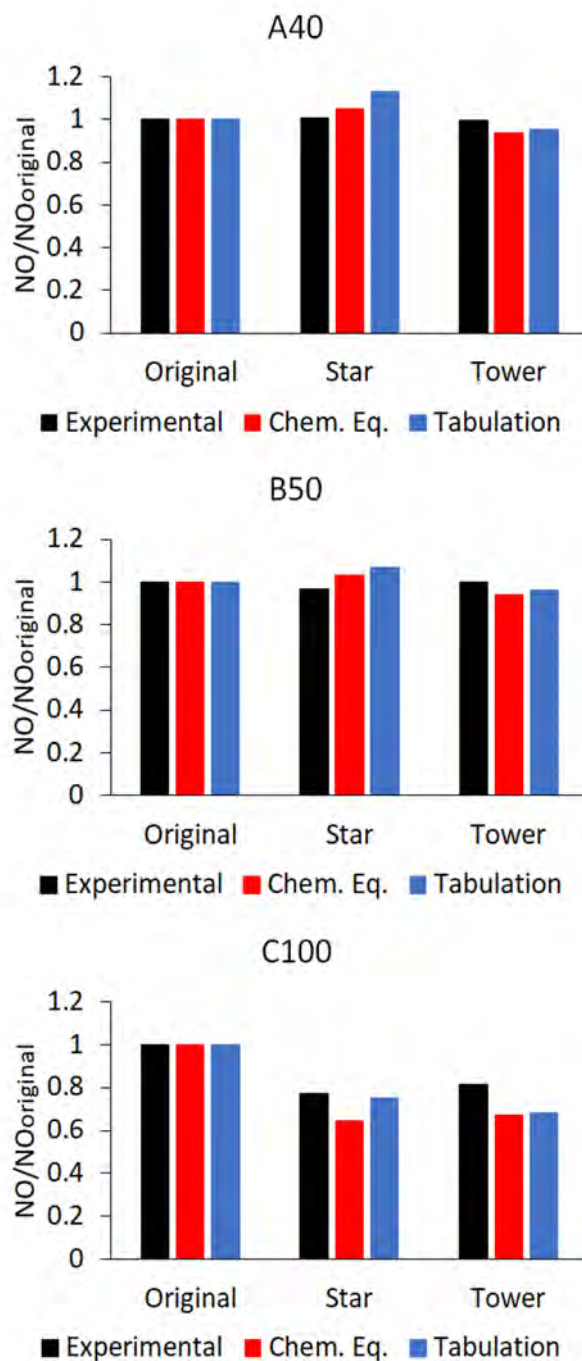

Figure 20. Comparison between computed and experimental NO emissions for the three investigated operating conditions. All values are normalized by the emissions obtained using the original piston.

Figure 21 reports a comparison of the computed and experimental CO emissions. Here, the absolute values are represented, since CO production mainly depends on the air-to-fuel ratio and not on the geometry. The results obtained by using tabulated kinetics were evaluated at the exhaust valve opening, whereas those calculated by using chemical equilibrium corresponded to the maximum value read in the combustion chamber, since, using this

approach, CO was almost completely oxidized to CO_2 during the expansion stroke. The computed emissions were in rather good agreement with the experimental results for the A40 and B50 conditions, whereas an underestimation of about 25% was obtained for the full-load operating condition. This aspect could be related to an underestimation of the burnt temperature in the CFD calculation, but more investigations are probably required.
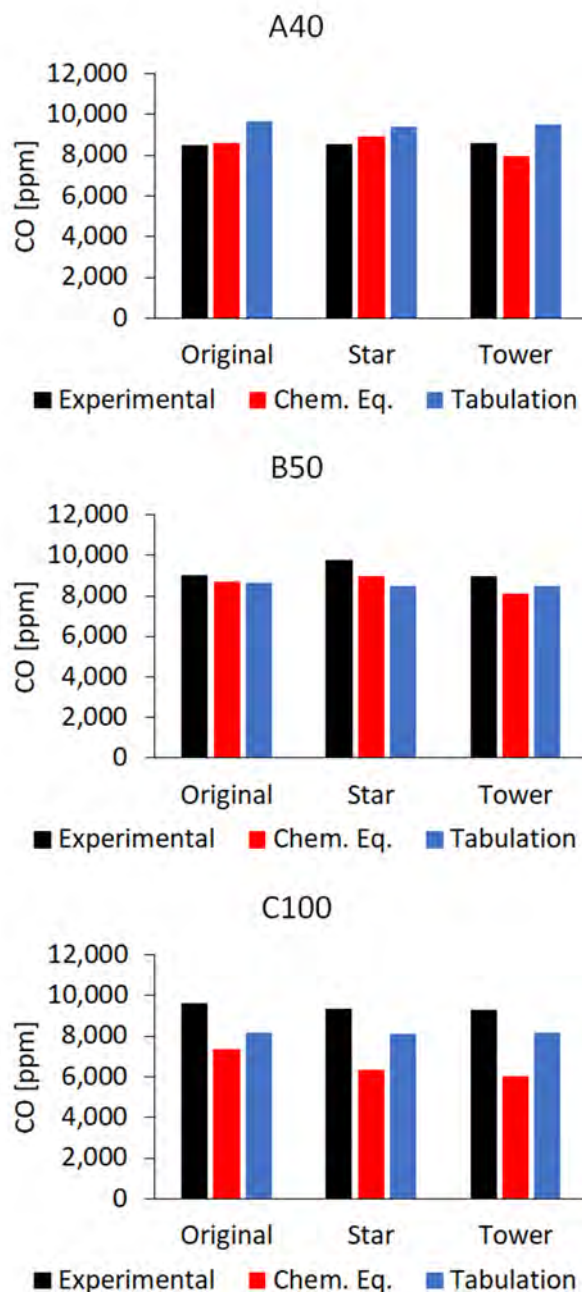

Figure 21. Comparison between the computed and experimental CO emissions for the three investigated operating conditions.

Finally, in Figure 22, a comparison between the computed and experimental CH_4 emissions for the B50 operating condition is reported on a logarithmic scale. Since piston crevices were not considered in the computational domain, it was not possible to obtain quantitative information on CH_4 emissions. In future work, the presence of crevices will also be considered to make a comparison between experimental and computed emissions for this greenhouse gas.
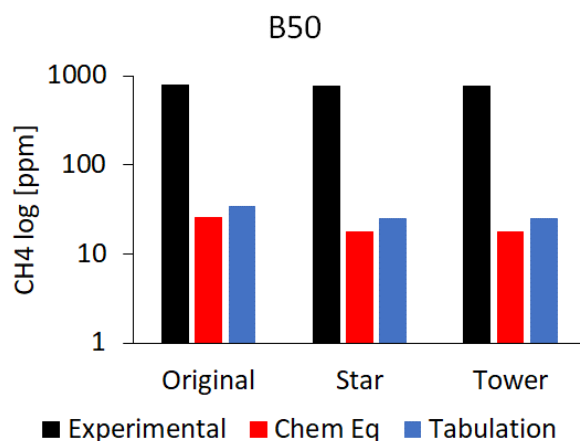
Figure 22. Comparison between the computed and experimental CH_4 emissions for the B50 operating condition on a logarithmic scale.

6. Conclusions and Future Development

The work presented in this paper was focused on the development and application of a combustion model for simulating spark-ignition engines operating with natural gas. The one-equation flame area model proposed by Weller was chosen due to its implicit formulation that ensures numerical stability and due to the limited number of tuning constants required.

The proposed approach was validated against a set of experimental data of a light-duty SI natural gas engine running at different engine speeds and loads. First, the model assessment was performed by using the original piston, and the results in terms of pressure, heat released, and pollutant emissions could be considered rather satisfactory for all of the tested conditions, even though some improvements are required, especially for high-load conditions. Then, two other piston bowl geometries were simulated under the same operating conditions to investigate the main differences in terms of turbulence generation and combustion evolution. The results were in rather good agreement with the experimental data, even though some discrepancies were visible, especially for low-load conditions. A more detailed description of the boundary conditions is probably required to improve the results. However, the proposed methodology was able to be successfully used for a preliminary investigation of the main advantages and disadvantages of changing the piston bowl geometry in a reasonable amount of time thanks to the use of the RANS approach. Concerning the effects of the new piston bowl geometries, no important improvements in terms of combustion efficiency were found, which was probably due to the very low (+4%) or null increase in turbulent kinetic energy during the intake and compression stroke and due to the greater heat losses (+20%) associated with the increased surface area of the new piston bowls.

Future works will focus their attention on alternative approaches to predicting the flame wrinkle factor and introducing crevice geometry in order to correctly predict HC emissions. Moreover, the proposed approach will also be used for the simulation of lean mixtures with more complex combustion systems, such as active prechambers and different low-carbon fuels, such as hydrogen.

Institutional Review Board Statement: Not applicable.

Informed Consent Statement: Not applicable.

Data Availability Statement: Not applicable.

Conflicts of Interest: The authors declare no conflict of interest.

Nomenclature

SI	Spark ignition
GHG	Greenhouse gas
CFD	Computational fluid dynamics
FAM	Flame area model
RANS	Reynolds-averaged Navier–Stokes
CNG	Compressed natural gas
TDC	Top dead center
EVO	Exhaust valve opening
CA10-90	Crank-angle interval needed to burn from 10% to 90% of the fuel mass
AHRR	Apparent heat release rate
ATDC	After top dead center
S_u	Unstrained laminar flame speed
S_t	Turbulent flame speed
u'	Turbulence intensity
L_t	Integral length scale
δ_f	Flame thickness
CFM	Coherent flamelet model
c	Combustion progress variable
b	Combustion regress variable
Σ	Flame surface density
LES	Large eddy simulation
Ξ	Flame wrinkling factor
IVC	Intake valve closure
ρ	Mixture density
ρ_u	Unburned mixture density
ρ_b	Burned mixture density
μ_t	Turbulent viscosity
$\dot{\omega}_{ign}$	Ignition source term
d_{ign}	Initial flame kernel diameter
Δt_{ign}	Time interval for the ignition source term
C_s	Strength coefficient of the ignition deposition model
I_0	Flame stretch coefficient
$I_{0,lam}$	Laminar flame stretch coefficient
$I_{0,turb}$	Turbulent flame stretch coefficient
f	Parameter for laminar-to-turbulent flame transition
r_k	Early flame kernel radius
$\mathcal{L}_u$	Markstein length
κ	Flame strain rate
λ	Taylor turbulence micro-scale
Ka	Karlovitz number
T_u	Unburned gas temperature
T_b	Burned gas temperature
δ	Heat conductivity
c_p	Heat capacity
Y_i	i-th species mass fraction
$Y_{u,i}$	i-th species mass fraction in the unburned state
$Y_{b,i}$	i-th species mass fraction in the burned state
h	Gas enthalpy
h_u	Unburned gas enthalpy
h_b	Burned gas enthalpy

References

1. Bae, C.; Kim, J. Alternative fuels for internal combustion engines. *Proc. Combust. Inst.* **2017**, *36*, 3389–3413. [CrossRef]
2. Pfoser, S.; Schauer, O.; Costa, Y. Acceptance of LNG as an alternative fuel: Determinants and policy implications. *Energy Policy* **2018**, *120*, 259–267. [CrossRef]
3. Gürbüz, H. Optimization of combustion and performance parameters by intake-charge conditions in a small-scale air-cooled hydrogen fuelled SI engine suitable for use in piston-prop aircraft. *Aircr. Eng. Aerosp. Technol.* **2021**, *93*, 448–456. [CrossRef]
4. Gürbüz, H.; Köse, S. A Theoretical Investigation on the Performance and Combustion Parameters in an Spark Ignition Engine Fueled With Different Shale Gas Mixtures. *J. Eng. Gas Turbines Power* **2021**, *143*, 061015. [CrossRef]
5. Sementa, P.; de Vargas Antolini, J.B.; Tornatore, C.; Catapano, F.; Vaglieco, B.M.; López Sánchez, J.J. Exploring the potentials of lean-burn hydrogen SI engine compared to methane operation. *Int. J. Hydrogen Energy* **2022**, *47*, 25044–25056. [CrossRef]
6. The European Commission. Reducing CO2 Emissions from Heavy-Duty Vehicles. Available online: https://ec.europa.eu/clima/policies/transport/vehicles/heavy_entab-0-0 (accessed on 12 April 2019).
7. US-EPA. EPA Emission Standards for Heavy-Duty Highway Engines and Vehicles. Available online: https://www.epa.gov/emission-standards-reference-guide/epa-emission-standards-heavy-duty-highway-engines-and-vehicles (accessed on 12 April 2019).
8. Paredi, D.; Lucchini, T.; D'Errico, G.; Onorati, A.; Golini, S.; Rapetto, N. *Gas Exchange and Injection Modeling of an Advanced Natural Gas Engine for Heavy Duty Applications*; SAE Paper; 2017-24-0026; SAE International: Warrendale, PA, USA, 2017.
9. Garg, M.; Ravikrishna, R. In-cylinder flow and combustion modeling of a CNG-fuelled stratified charge engine. *Appl. Therm. Eng.* **2019**, *149*, 425–438. [CrossRef]
10. Zhou, H.; Li, X.; Lee, C.F.F. Investigation on soot emissions from diesel-CNG dual-fuel. *Int. J. Hydrogen Energy* **2019**, *44*, 9438–9449. [CrossRef]
11. Stefana, E.; Marciano, F.; Alberti, M. Qualitative risk assessment of a Dual Fuel (LNG-Diesel) system for heavy-duty trucks. *J. Loss Prev. Process Ind.* **2016**, *39*, 39–58. [CrossRef]
12. Pavel, N.; Barwinkel, M.; Heinz, P.; Bruggemann, D.; Dearden, G.; Croitoru, G.; Grigore, O.V. Laser ignition—Spark plug development and application in reciprocating engines. *Prog. Quantum Electron.* **2018**, *58*, 1–32. [CrossRef]
13. Lo, A.; Frat, F.; Domingues, E.; Lacour, A.; Lecordier, B.; Vervisch, P.; Cessou, A. Nanosecond pulsed discharge in a propane-air mixture: Ignition and energy deposition. *Proc. Combust. Inst.* **2017**, *36*, 4087–4094. [CrossRef]
14. Hall, J.; Bassett, M.; Hibberd, B.; Streng, S. Heavily Downsized Demonstrator Engine Optimised for CNG Operation. *SAE Int. J. Engines* **2016**, *9*, 2250–2261. [CrossRef]
15. Kakaee, A.H.; Nasiri-Toosi, A.; Partovi, B.; Paykani, A. Effects of piston bowl geometry on combustion and emissions characteristics of a natural gas/diesel RCCI engine. *Appl. Therm. Eng.* **2016**, *102*, 1462–1472. [CrossRef]
16. Heuser, P. Diesel-Based Natural Gas Engines for Commercial Applications. In Proceedings of the Internationales Wiener Motorensymposium, Vienna, Austria, 8–9 May 2014.
17. Wohlgemuth, S.; Roesler, S.; Wachtmeister, G. Piston Design Optimization for a Two-Cylinder Lean-Burn Natural Gas Engine—3D-CFD-Simulation and Test Bed Measurements. In Proceedings of the SAE 2014 World Congress & Exhibition, Detroit, MI, USA, 8–10 April 2014. [CrossRef]
18. Wu, C.; Deng, K.; Wang, Z. The effect of combustion chamber shape on cylinder flow and lean combustion process in a large bore spark-ignition CNG engine. *J. Energy Inst.* **2016**, *89*, 240–247. [CrossRef]
19. Peters, N. *Turbulent Combustion*; Cambridge University Press: Cambridge, UK, 2000.
20. Marble, F.E.; Broadwell, J.E. *The Coherent Flame Model for Turbulent Chemical Reactions*; Technical Report; TRW Defense and Space Systems Group: Huntsville, AL, USA , 1977.
21. Veynante, D.; Lacas, F.; Maistret, E.; Candel, S.M. Coherent Flame Model for Non-Uniformly Premixed Turbulent Flames. In *Turbulent Shear Flows 7*; Springer: Berlin/Heidelberg, Germany, 1991; pp. 367–378.
22. Peters, N. The turbulent burning velocity for large-scale and small-scale turbulence. *J. Fluid Mech.* **1999**, *384*, 107–132. [CrossRef]
23. Ewald, J.; Peters, N. A Level Set Based Flamelet Model for the Prediction of Combustion in Spark-Ignition Engines. In Proceedings of the Multi-Dimensional Engine Modeling Meeting 2005, San Francisco, CA, USA, 15–18 August 2005.
24. Herrmann, M. Refined Level Set Grid method for tracking interfaces. In *Annual Research Briefs*; Center for Turbulence Research: Stanford, CA, USA, 2005.
25. d'Adamo, A.; Breda, S.; Fontanesi, S.; Cantore, G. LES Modelling of Spark-Ignition Cycle-to-Cycle Variability on a Highly Downsized DISI Engine. *SAE Int. J. Engines* **2015**, *8*, 2029–2041. [CrossRef]
26. Colin, O.; Benkenida, A. The 3-Zones Extended Coherent Flame Model (ECFM3Z) for Computing Premixed/Diffusion Combustion. *Oil Gas Sci. Technol.* **2004**, *59*, 593–609. [CrossRef]
27. Tan, Z.; Reitz, R.D. *Modeling Ignition and Combustion in Spark-Ignition Engines Using a Level-Set Method*; SAE Paper; 2003-01-0722; SAE International: Warrendale, PA, USA, 2003.
28. Lucchini, T.; Cornolti, L.; Montenegro, G.; D'Errico, G.; Fiocco, M.; Teraji, A.; Shiraishi, T. *A Comprehensive Model to Predict the Initial Stage of Combustion in SI Engines*; SAE Paper; 2013-01-1087; SAE International: Warrendale, PA, USA, 2013.
29. Duclos, J.M.; Colin, O. Arc and Kernel Tracking Ignition Model for 3D Spark-Ignition engine calculations. In Proceedings of the COMODIA 2001 Conference, Nagoya, Japan, 1–4 July 2001.

30. Dahms, R.N.; Drake, M.C.; Fansler, T.D.; Kuo, T.W.; Peters, N. Understanding ignition processes in spray-guided gasoline engines using high-speed imaging and the extended spark-ignition model SparkCIMM. Part A: Spark channel processes and the turbulent flame front propagation. *Combust. Flame* **2011**, *158*, 2229–2244. [CrossRef]

31. Pitsch, H. A consistent level set formulation for large-eddy simulation of premixed turbulent combustion. *Combust. Flame* **2005**, *143*, 587–598. [CrossRef]

32. Spalding, D.B. Development of the eddy-break-up model of turbulent combustion. *Symp. (Int.) Combust.* **1977**, *16*, 1657–1663. [CrossRef]

33. Weller, H.G. *The Development of a New Flame Area Combustion Model Using Conditional Averaging*; Thermo-Fluids Section Report TF 9307; Imperial College of Science, Technology and Medicine: London, UK, 1993.

34. Choi, C.R.; Huh, K.Y. Development of a Coherent Flamelet Model for a Spark- Ignited Turbulent Premixed Flame in a Closed Vessel. *Combust. Flame* **1998**, *114*, 336–348. [CrossRef]

35. Toninel, S.; Forkel, H.; Frank, T.; Durst, B.; Hasse, C.; Linse, D. Implementation and Validation of the G-equation Model Coupled with Flamelet Libraries for Simulating Premixed Combustion in I.C. Engines. *SAE Int. J. Engines* **2009**, *2*, 674–690. [CrossRef]

36. Gulder, O.L. Turbulent Premixed Flame Propagation Models for Different Combustion Regimes. In Proceedings of the Twenty-Third Syposium on Combustion (International), Orléans, France, 22–27 July 1990; pp. 743–750.

37. Maly, R.R.; Herweg, R. *A Fundamental Model for Flame Kernel Formation in SI Engines*; SAE Paper; 922243; SAE International: Warrendale, PA, USA, 1992.

38. Lucchini, T.; D'Errico, G.; Onorati, A.; Bonandrini, G.; Venturoli, L.; Gioia, R.D. Development and Application of a Computational Fluid Dynamics Methodology to Predict Fuel-Air Mixing and Sources of Soot Formation in Gasoline Direct Injection Engines. *Int. J. Engine Res.* **2014**, *15*, 581–596. [CrossRef]

39. Lucchini, T.; Torre, A.D.; D'Errico, G.; Onorati, A.; Maes, N.; Somers, L.; Hardy, G. A comprehensive methodology for computational fluid dynamics combustion modeling of industrial diesel engines. *Int. J. Engine Res.* **2017**, *18*, 26–38. [CrossRef]

40. Lucchini, T.; Torre, A.D.; D'Errico, G.; Montenegro, G.; Fiocco, M.; Maghbouli, A. *Automatic Mesh Generation for CFD Simulations of Direct-Injection Engines*; SAE Paper; 2015-01-0376; SAE International: Warrendale, PA, USA, 2015.

41. Sforza, L.; Lucchini, T.; Gianetti, G.; D'Errico, G. Development and Validation of SI Combustion Models for Natural-Gas Heavy-Duty Engines. In Proceedings of the 14th International Conference on Engines & Vehicles, Naples, Italy, 15–19 September 2019. [CrossRef]

42. Sforza, L.; Lucchini, T.; Gianetti, G.; D'Errico, G.; Onofrio, G.; Beatrice, C.; Tunestal, P. A 3D-CFD Methodology for Combustion Modeling in Active Prechamber SI Engines Operating with Natural Gas. In Proceedings of the WCX SAE World Congress Experience, Detroit, MI, USA, 5–7 April 2022. [CrossRef]

43. Lucchini, T.; D'Errico, G.; Jasak, H.; Tukovic, Z. *Automatic Mesh Motion with Topological Changes for Engine Simulation*; SAE Paper; 2007-01-0170; SAE International: Warrendale, PA, USA, 2007.

44. Lucchini, T.; D'Errico, G.; Brusiani, F.; Bianchi, G. A Finite-Element Based Mesh Motion Technique for Internal Combustion Engine Simulations. In Proceedings of the COMODIA 2008, Sapporo, Japan, 28–31 July 2008; MS2-3.

45. Yang, X.; Solomon, A.; Kuo, T. Ignition and Combustion Simulations of Spray-Guided SIDI Engine using Arrhenius Combustion with Spark-Energy Deposition Model. In Proceedings of the SAE 2012 World Congress & Exhibition, Detroit, MI, USA, 24–26 April 2012. [CrossRef]

46. Sforza, L.; Lucchini, T.; Onorati, A.; Zhu, X.; Lee, S. Modeling Ignition and Premixed Combustion Including Flame Stretch Effects. In Proceedings of the WCX™ 17: SAE World Congress Experience, Detroit, MI, USA, 4–6 April 2017. [CrossRef]

47. Bowman, C.; Hanson, R.; Davidson, D.; Gardiner, W.J.; Lissianski, V.; Smith, G.; Golden, D.; Frenklach, M.; Goldenberg, M. GRI-Mech 2.1. 1996. Available online: http://combustion.berkeley.edu/gri-mech/version30/text30.html (accessed on 25 October 2019).

48. Lucchini, T.; D'Errico, G.; Onorati, A.; Frassoldati, A.; annd Gilles Hardy, A.S. Modeling Non-Premixed Combustion Using Tabulated Kinetics and Different Flame Structure Assumptions. *SAE Int. J. Engines* **2017**, *2*, 593–607. [CrossRef]

49. Erickson, W.D.; Prabhu, R.K. Rapid computation of chemical equilibrium composition: An application to hydrocarbon combustion. *AIChE J.* **1986**, *32*, 1079–1087.

50. Gürbüz, H.; Buran, D.; Akçay, H.T. An experimental study on performance and cyclic variations in a spark ignition engine fuelled with hydrogen and gasoline. *J. Therm. Sci. Technol.* **2013**, *33*, 33–41.